Smart Structures and Systems, *Vol. 24, No. 2 (2019) 157-171*
DOI: https://doi.org/10.12989/sss.2019.24.2.157

Displacement-recovery-capacity of superelastic SMA fibers reinforced cementitious materials

Eunsoo Choi[*1], Behzad Mohammadzadeh[**1], Jin-Ha Hwang[2a] and Jong-Han Lee[3b]

[1]*Department of Civil Engineering, Hongik University, Seoul 04066, Korea*
[2]*Department of Material Science and Engineering, Hongik University, Seoul 04066, Korea*
[3]*Department of Civil Engineering, Inha University, Incheon 22212, Korea*

(Received August 11, 2018, Revised February 22, 2019, Accepted February 27, 2019)

Abstract. This study investigated the effects of the geometric parameters of superelastic shape memory alloy (SE SMA) fibers on the pullout displacement recovering and self-healing capacity of reinforced cementitious composites. Three diameters of 0.5, 0.7 and 1.0 mm and two different crimped lengths of 5.0 and 10.0 mm were considered. To provide best anchoring action and high bond between fiber and cement mortar, the fibers were crimped at the end to create spear-head shape. The single fiber cement-based specimens were manufactured with the cement mortar of a compressive strength of 84 MPa with the square shape at the top and a dog-bone shape at the bottom. The embedded length of each fiber was 15 mm. The pullout test was performed with displacement control to obtain monotonic or hysteretic behaviors. The results showed that pullout displacements were recovered after fibers slipped and stuck in the specimen. The specimens with fiber of larger diameter showed better displacement recovering capacity. The flag-shaped behavior was observed for all specimens, and those with fiber of 1.0 mm diameter showed the clearest one. It was observed that the length of fiber anchorage did not have a significant effect on the displacement recovery, pullout resistance and self-healing capacity.

Keywords: cement-based composites; superelastic SMA fibers; self-healing capacity; crack-closing capacity; displacement recovery; flag-shaped behavior

1. Introduction

Cementitious materials, including mortar and concrete, are widely used for civil structures because of their comparatively low cost, flexibility of application, and easy composition with other components (Kim and Cho 2018, Mohammadzadeh and Noh 2017, Jang and An 2018, Choi *et al.* 2015, Yang *et al.* 2017). However, these materials generally display the disadvantage of low tensile strength; thus, they are prone to cracking due to external loading (Kim *et al.* 2012, Shokri and Nanni 2014, Mohammadzadeh *et al.* 2012). The first approach to overcome this problem is to reinforce the tensile regions of cementitious structural members using conventional steel reinforcing bars (Dyshlyuk *et al.* 2017, Mohammadzadeh and Noh 2016, Mohammadzadeh and Noh 2014, Kang *et al*. 2018, Mohammadzadeh and Noh 2015). This method works well to provide resistance against tension due to bending; however, steel reinforcement cannot provide crack-closing or recovery of displacement after cracking in members of cementitious materials (Gribniak *et al.* 2018, Truong *et al.* 2017, Mohammadzadeh and Noh 2019, Aguirre and Montejo 2014). During the past few decades, employing smart materials, such as shape memory alloys has been adopted as an alternative for providing self-repairing and crack-closing capacities in composites and cementitious materials (Kim *et al.* 2014, Qiu *et al*. 2018, Hadi and Akbari 2016, Jiang *et al.* 2015). Shape memory alloys (SMAs) possess the unique properties of the shape memory effect and superelasticity, which are useful characteristics for composite structures (Kim *et al.* 2006, Choi *et al*. 2016, Mehrabi and Karamooz 2015). The shape memory effect which induces recovery stress can be used to provide prestressing and crack-closing. For this purpose, wires or bars made of the SMA have been employed (Baghani *et al.* 2012, Schrooten *et al.* 2002, Pereiro-Barcelo and Bonet 2017, Shahyerdi *et al.* 2016, Wang *et al*. 2014, Feng and Sun 2007). In these cases, end-anchoring has been used to hold the wires or bars, or couplers are used to connect them to steel reinforcing bars, and electric power is supplied to increase the temperature of the SMAs to induce the shape memory effect; however, the end-anchoring, coupler, and electric power supply are troublesome. Recently, SMA short fibers using the shape memory effect have been applied to achieve prestressing and crack-closing in mortar beams (Choi *et al.* 2016, Choi *et al.* 2015, Liu *et al.* 2015). SMA short fibers can be used without any interface to steel reinforcing bars in reinforced concrete (RC) beams. SMA short fibers can be placed at a specific location or randomly

∗Corresponding author, Professor
E-mail: eunsoochoi@hongik.ac.kr
** Ph.D.
E-mail: Behzad.alb@gmail.com
[a] Professor
E-mail: jhwang@hongik.ac.kr
[b] Associate Professor
E-mail: jh.lee@inha.ac.kr

http://www.techno-press.com/journals/sss&subpage=7
ISSN: 1738-1584 (Print), 1738-1991 (Online)

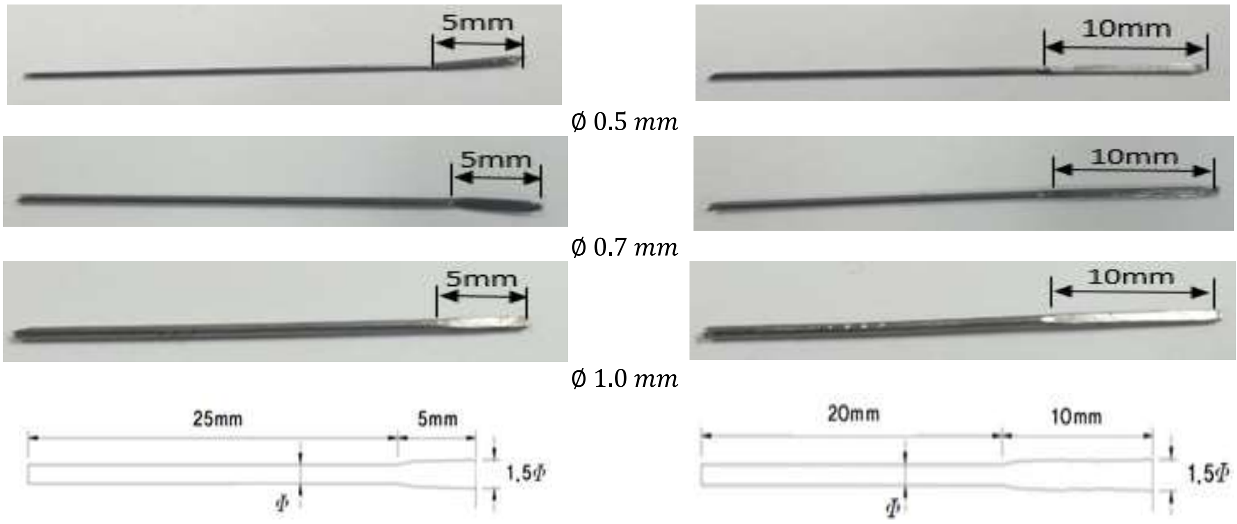

Crimped length of 5.0 mm

Crimped length of 10.0 mm

Fig. 1 Illustrations and photographs of spearhead SMA fibers

distributed in mortar or concrete. In such cases, electronic power cannot be used to heat the SMA fibers; therefore, heat guns or flame are used to increase the temperature of the SMA short fibers. NiTi SMA short fibers placed at the bottom of the mortar beams can successfully provide a prestressing force which induces up-lift displacement of the beam when the SMA fibers are heated before cracking occurs. When the SMA fibers are heated after cracking, the recovery stress closes the opened crack and supplies closing force at the crack-surface. If an adhesive such as epoxy is applied on the crack-surface, the tensile strength at the crack is recovered and, thus, the crack is repaired.

Superelastic (SE) SMAs are also applied to reinforced concrete (RC) structures to provide self-centering or self-repairing capacity without any external energy supply. For SE SMA applications, wires or bars have been employed for beams, beam-column connections, and bottom connection of RC columns (Choi *et al.* 2015, Kabir *et al.* 2016, Oudah and El-Hacha 2017, Li *et al.* 2015, Abou-Elfath 2017, Choi *et al.* 2018). They were successful to recover deflection of beams due to external loadings when the loadings were removed, and they also increased the self-centering capacity of conventional columns. After that, SE SMA short fiber was applied to automatically close cracks in mortar or concrete beams when external loading was removed. Several pullout tests of SE SMA fibers have been conducted with various end shapes of the fibers (Choi *et al.* 2018, Horney *et al*. 2012, Choi *et al.* 2017). In addition, SE SMA short fibers have been applied to mortar beams to obtain the capacity to self-close cracks (Choi *et al.* 2018, Farmani and Ghassemieh 2016). However, these attempts were not very successful; the SE SMA fibers partially recovered the deflection of the beams with unloading. In the pullout tests, the SE SMA fibers showed residual displacement. This result was different from those obtained for beams using wires or bars of the SE SMA. Wires or bars of SE SMA in beams were perfectly anchored at the ends. Thus, they were deformed without slip and showed almost perfect deflection recovery capacity. However, for the SE SMA fibers, the ends of the fibers were embedded in mortar or concrete, and the anchorage was not perfect; thus, it allowed slipping at the ends for which displacement was not recovered.

The previous studies used different anchoring types with fibers of one diameter, and they discussed the pullout resistance or recovering deflection of the beams according to the anchoring types. Therefore, this study aims to investigate the pullout behavior of SE SMA fibers with various diameters. However, the SE SMA was made from a batch; hence, the fibers with different diameters were expected to show the same stress–strain curves, although they would be expected to show different tensile forces. For the purposes of this study, three different diameters of SE SMA fibers were prepared, and monotonic and hysteretic pullout tests were conducted. The monotonic pullout test is employed to investigate the bond behavior between fiber and matrix while the hysteretic pullout test is employed to assess the self-centering and displacement recovery of the SMA fibers embedded in cementitious structures.

2. Preparation for experiment

2.1 Types of superelastic SMA fiber

In this study, two types of SE SMA fibers considering different crimped-end lengths of 5.0 and 10.0 mm were prepared, while each type included three types of fibers with various diameters of 0.5, 0.7, and 1.0 mm. In total, this study considered six types of SE SMA fibers to investigate the effects of the geometric parameters, diameter, and crimped length on the pullout behavior of SE SMA fibers. The fibers were expected to have similar properties even with various diameters. Applying external tensile load can result in deformation of the austenitic SMA fiber and activation of superelasticity. Austenite to detwinned martensite phase transformation occurs upon loading following elastic deformation of SMA. Energy dissipation occurs through the unloading path, which is different from

(a) 0.5 mm (b) 0.7 mm (c) 1.0 mm

Fig. 2 Photographs of SMA fiber diameter measuring instruments

Fig. 3 Typical tensile test setup for the hysteretic tensile stress–strain behavior of SMA wires

the loading path, during detwinned martensite to austenite phase transformation. Phase transformation starts when the stress induced in SMA fiber reaches the upper plateau stress. The fibers considered in this study were categorized in two main batches with respect to crimped-end length: 1) 5.0-mm length and 2) 10.0-mm length. Each batch included three types of SMA fibers that had different diameters of 0.5, 0.7, and 1.0 mm. The embedment length of each fiber was 15 mm. The general shapes of the SMA fibers and their corresponding dimensions are presented in Fig. 1.

To perform a set of precise experiments, the diameters of the SMA fibers needed to be measured using the measuring machine shown in Fig. 2 with typical measurements of representative SMA fibers of each diameter: 0.5 mm, 0.7 mm, and 1.0 mm. To enable analysis and interpretation of the results, the hysteretic tensile behavior of SMA wires of different diameters should be known and accessible.

2.2 Hysteretic tensile stress-strain behavior

To perform the pullout tests and to investigate the behaviors and responses of the SMA short fibers, the SMA wire properties, namely, upper plateau stress, lower plateau stress, hardening behavior, and strain limits should be known. For this aim, an SMA wire tensile test under cyclic loading was performed, and responses of the SMA wire were recorded to draw the hysteretic tensile stress–strain curve. A photograph of the typical SMA wire tensile test setup is shown in Fig. 3 to provide a better understanding of the test process and environment.

The experiment was performed at the temperature of 25℃, which is higher than the temperature of A_f =18.0℃ of the SMA. The hysteretic stress–strain curves of SE SMA wires with diameters of 0.5, 0.7, and 1.0 mm are shown in Fig. 2. The peak values of the upper plateau stress at the beginning were 655, 653, and 620 MPa for wires of 0.5, 0.7, and 1.0 mm diameter, respectively. The flag-shaped behavior of the SE SMA wires appears after the peak point of upper plateau stress is achieved. Thus, the importance of having hysteretic tensile stress–strain curve of SMA wires from which the short SMA fibers are going to be created is clear.

The secant elastic modulus of the SMA wire of 0.5 mm diameter shown in Fig. 4(a) is 44.9 GPa. The SMA started phase transformation at a strain of 1.58% and the corresponding stress of 655 MPa. The lower plateau stress

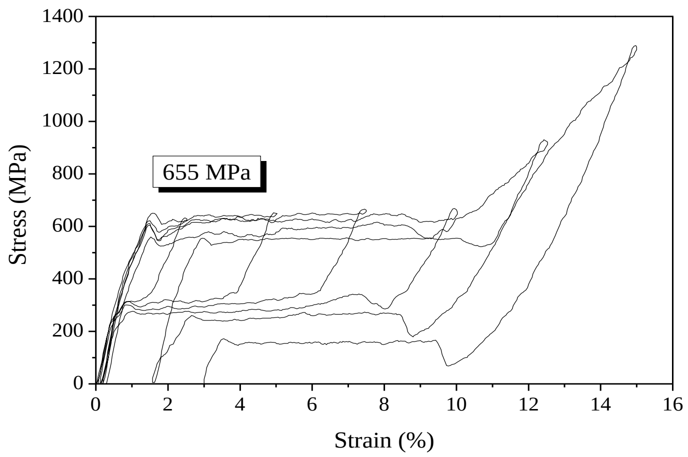

(a) SE SMA wire of 0.5 mm diameter

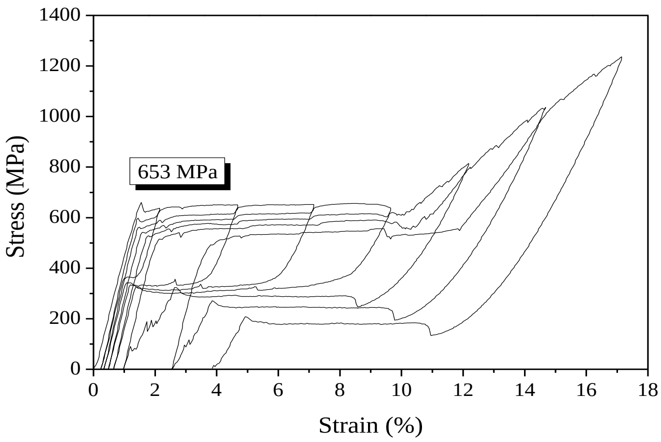

(b) SE SMA wire of 0.7 mm diameter

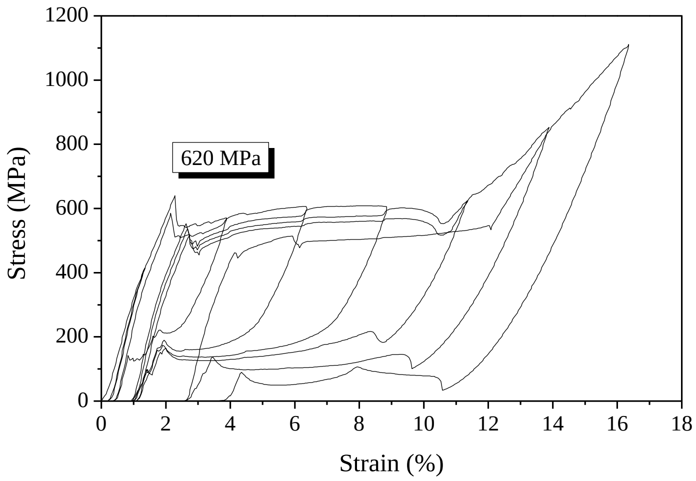

(c) SE SMA wire of 1.0 mm diameter

Fig. 4 Hysteretic tensile stress–strain curve of superelastic SMA wires of different diameters

during unloading at a 1.15% strain was 315 MPa. In the graph, stress-induced-martensite (SIM) hardening can be observed. The loading path to a 15% strain showed hardening behavior after a 10.5% strain. This indicates stress-induced martensite (SIM) hardening, for which the stress onset was 658.9 MPa. The residual strain of 0.025% remained due to unloading from the 2.53% strain, and it slightly increased as unloading deformation increased. The

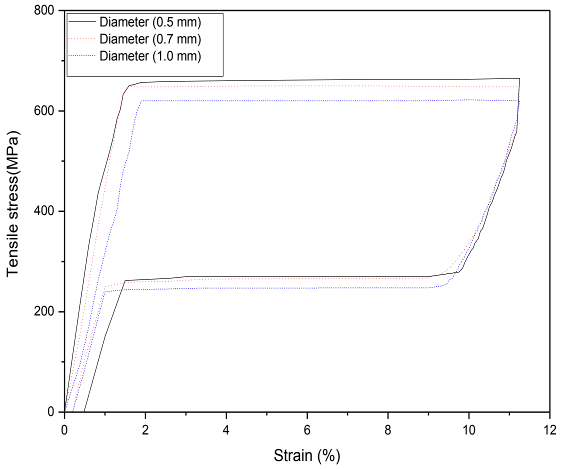

(a) Tensile stress-strain envelope

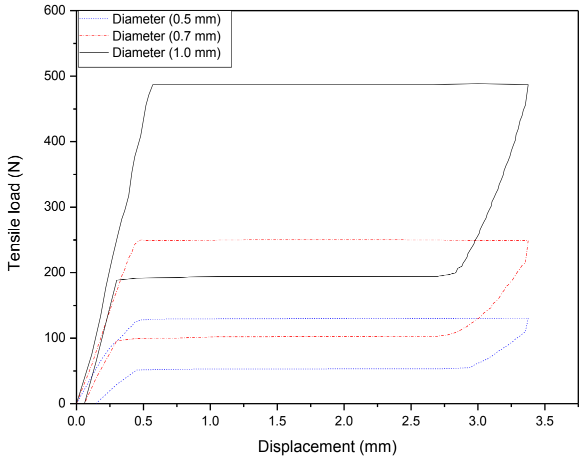

(b) Tensile load-displacement envelope

Fig. 5 Comparative graph presenting stress–strain and load-displacement envelopes of SMA wires

SMA wire of 0.7 mm diameter shown in Fig. 4(b) had the secant modulus of elasticity of 35.8 GPa. The phase transformation began at the strain of 1.55% and the stress of 653 MPa. The lower plateau stress of 358.4 MPa could be observed at 1.03% strain. SIM hardening occurred at the strain of 10.55% and the corresponding onset stress of 656.3 MPa. The graph regarding SMA wire of 1.0 mm diameter presented in Fig. 4(c) showed a modulus of elasticity of 25.3 GPa. The phase transformation could be observed at 2.28% strain and 620 MPa stress. The lower plateau stress of 142.2 MPa occurred at 0.83% strain. As the transformation to martensite phase completed, elastic and plastic deformations were observed. The elastic deformation could be recovered through unloading after the completion of transformation, but the plastic deformation remained.

2.3 Comparison of tensile stress-strain behavior envelopes

A comparative graph presenting the envelopes of the load-displacement relation of SMA wires is provided in Fig. 5. It provides a good insight into the function of each type of wire when a cyclic pullout load was applied. It would be helpful for choosing the most appropriate type for the desired research work or engineering application.

As seen in Fig. 5, all the SE SMA wires considered in this study showed good strain recovery and beginning upper plateau stresses higher than 600 MPa. However, SMA wires having diameters of 0.5 and 0.7 mm showed very similar upper plateau stress, while the wire of 1.0 mm showed a lower stress. The corresponding forces were 128.6, 251.3, and 487 N for 0.5, 0.7, and 1.0 mm diameter, respectively. Since the force is proportional to the area of the wire, the force of 128.3 N of the 0.5 mm diameter wire was almost a quarter of that of the 1.0 mm diameter wire. The graphs in Fig. 5 suggest that the SMA fibers of 0.5 and 0.7 mm are more appropriate for practical applications, especially for research, because the specimens are small. SMA fibers of 1.0 mm diameter and larger can be employed for large structures and engineering applications. For these uses, the appropriate functions can be obtained with large diameter fibers.

3. Pullout test

3.1 Specimen preparation

The effects of SMA fiber diameter and crimped-end length on the pullout resistance were investigated through the pullout test. For this aim, the cement type III was considered for the matrix. Silica sand with 0.22 mm particle size was mixed with cement in the sand-to-cement ratio of 1.0. Accordingly, dog-bone shaped specimens were cast using a cementitious mortar of 84 MPa having the characteristics defined by weight ratio as shown in Table 1.

A Hobart-type mixer with a capacity of 15 L was used in mixing the mortar matrix. Cement was first mixed with fly ash, and silica sand with 0.22 mm particle size in a sand-to-cement ratio of 1.0 for 5 min in a dry condition, after which water was added slowly and mixed for 3 to 4 min. A high-range water-reducing agent was also added to the slurry, which was mixed for an additional 3 min. When the mortar mixture showed suitable workability, it was ready to be poured into the molds. The samples were cast such that each specimen contained one embedded SMA fiber with an embedded length of 15.0 mm. The specimen height was 71.5 mm. To fabricate the specimens, the cement matrix was poured into molds and fibers were embedded in the cement matrix. Each specimen had a square shape at the top, and a dog-bone shape was formed at the bottom to resist against pulling force. Illustrations of representative specimens and photographs of real molds and specimens created and used in this study are provided in Fig. 6. It was possible to fabricate 10 specimens at one time by using the mold shown in Fig. 6(c).

Table 1 Weight ratio of the mortar matrix components

Material	Cement (type III)	Silica Fume	Silica Sand	Fly ash	Super-plasticizer	Water	Strength (MPa)
Weight ratio	0.80	0.07	1.00	0.20	0.04	0.26	84

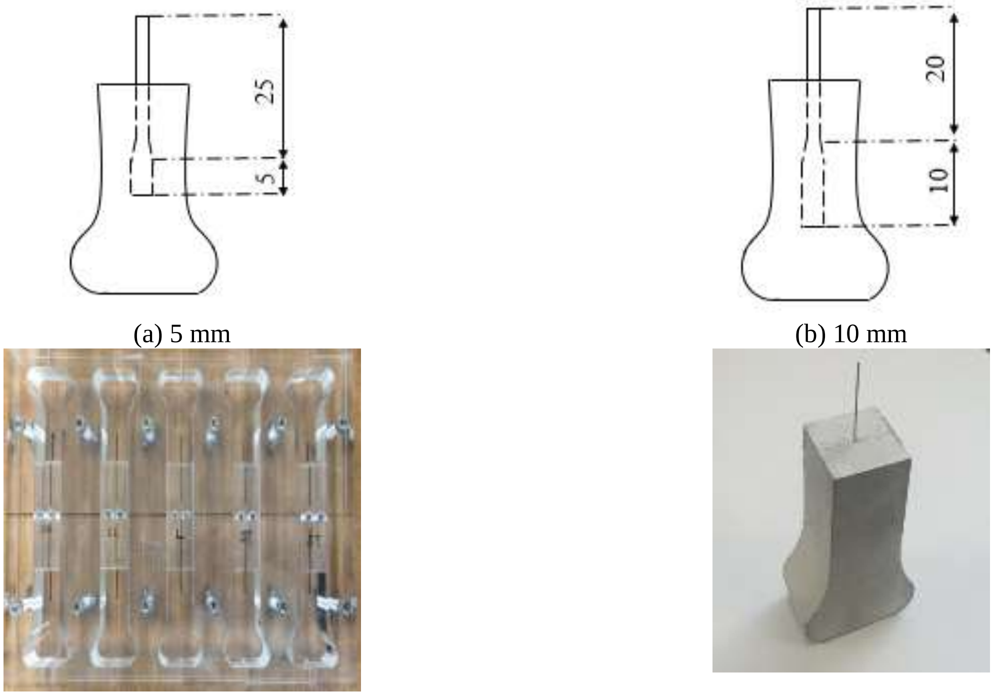

(a) 5 mm (b) 10 mm

(c) Mold (d) Specimen

Fig. 6 Illustration of typical specimens and photographs of mold and specimen

3.2 Experimental set-up

To investigate the effects of the geometric parameters of superelastic SMA fibers on pullout behavior, a series of experiments was designed. This study considered crimped-end (spearhead) fibers because, in previous studies, it has been documented that they can provide the best pullout resistance and show flag-shaped behavior (Choi *et al.* 2018) Each specimen contained only one embedded SMA fiber with the embedded length of 15 mm.

3.3 Test procedure

The pullout test was conducted under the condition of displacement control with a loading speed of 1.0 mm/min. The pullout load applied to the fiber and the strain was increased until 1 mm displacement occurred, then the load was released. Thereafter, 2% strain was added to the previous strain up to failure. A half-circular holder gripped the bottom of the specimen, and the fiber was pulled out by an actuator. The applied force was measured by a load cell placed on the top of the machine cross-head, and the slip between the fiber and the mortar was measured by a linear voltage displacement transducer (LVDT) mounted on the specimen. Displacement control with a speed of 1.0 mm/min was applied while the sampling rate was 5.0 Hz. Fig. 7 shows the pullout test device and setup for a single fiber specimen.

Upon application of the tensile load, the SE SMA fiber showed deformation and slip. Therefore, superelasticity was activated and flag-shaped behavior could be observed. After the SE SMA fiber bore elastic deformation, the austenite to martensite phase transformation occurred during loading. Through unloading, the martensite phase transformed to austenite and led to energy dissipation because of the disparate paths of loading and unloading.

Typical photographs of specimens before and after the pullout test are provided in Fig. 8. A single fiber specimen in the pullout test machine before the load was applied is shown in Fig. 8(a). The specimen after completion of loading griped in the pullout test machine is shown in Fig. 8(b). The released specimen is shown in Fig. 8(c). In Figs. 8(b) and 8(c), a crack can be observed at the top of the specimen. This crack could reduce the bond strength of the fiber and mortar, so the fiber carrying tensile load decreased. Therefore, after the fiber slipped, the sustainable pullout stress decreased. Through a series of pullout tests, the hysteretic pullout behavior of the SE SMA fibers embedded in cementitious mortars was assessed.

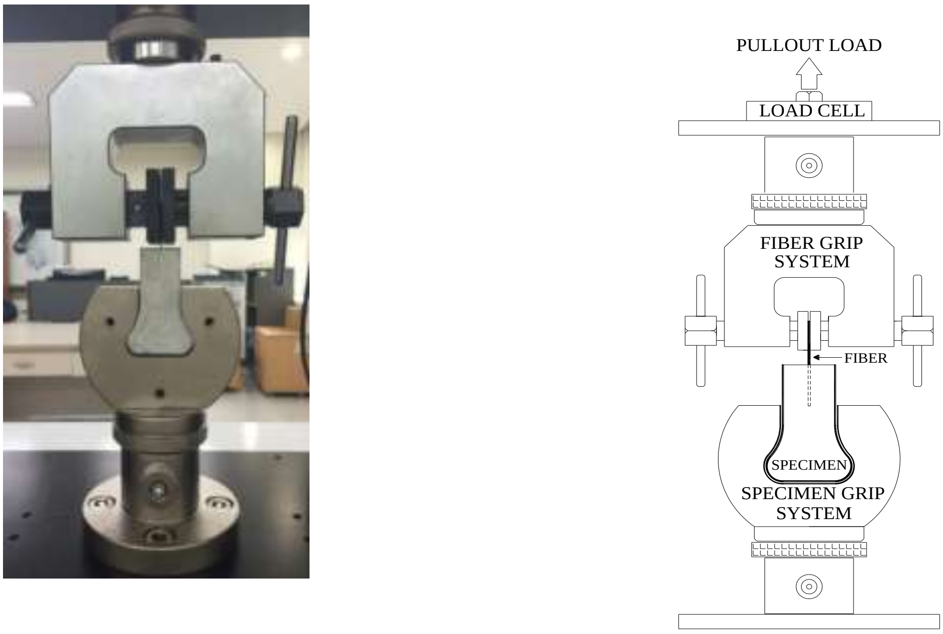

(a) Picture (b) Illustration

Fig. 7 Photograph and illustration of pullout test machine

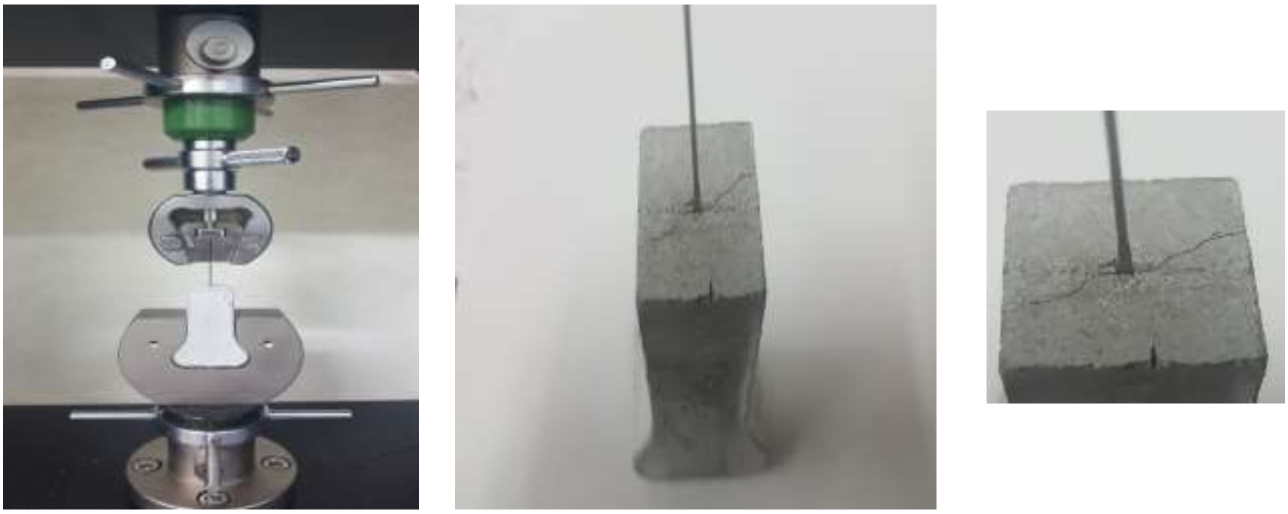

(a) Gripped (b) Released (c) pulled out fiber

Fig. 8 Photos of a gripped and released the single-fiber specimen

4. Pullout test results

This study investigated the effects of diameter and crimped-end length of superelastic SMA fibers on the pullout resistance. For this purpose, pullout tests were conducted on single-fiber specimens. Well-measured data from the test was obtained, and the hysteretic pullout behavior results of each type of specimen are presented in the form of a graph. In the following subsections, the pullout behavior of each type of SE SMA fiber is comprehensively discussed in two main batches with crimped lengths of 5 and 10 mm.

4.1 Crimped length of 5 mm

A pullout test was conducted on each single-fiber specimen, and the pullout behavior of each type of fiber was observed. The results are presented in the form of combined force-displacement-stress curves, as shown in Fig. 9. It is appropriate to note that displacement is the sum of fiber slip and deformation. The abscissa indicates the displacement, while ordinate shows the pullout load on the left side and pullout stress on the right side. They were calculated on the straight parts of the fibers.

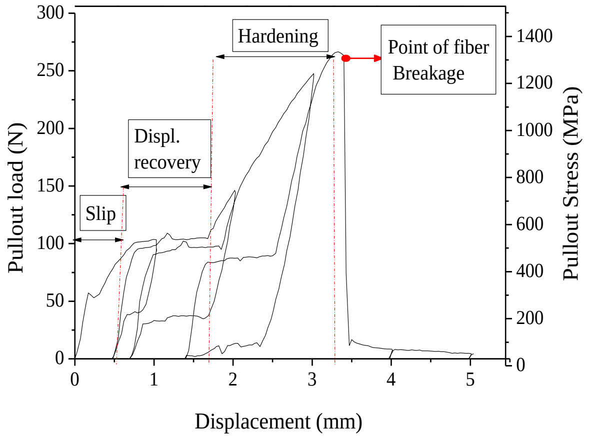

(a) Diameter of 0.5 mm

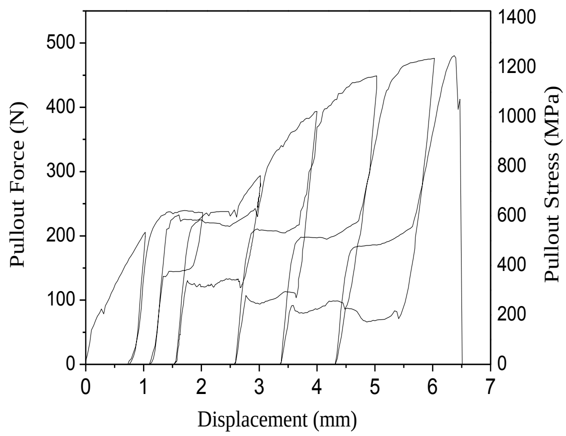

(b) Diameter of 0.7 mm

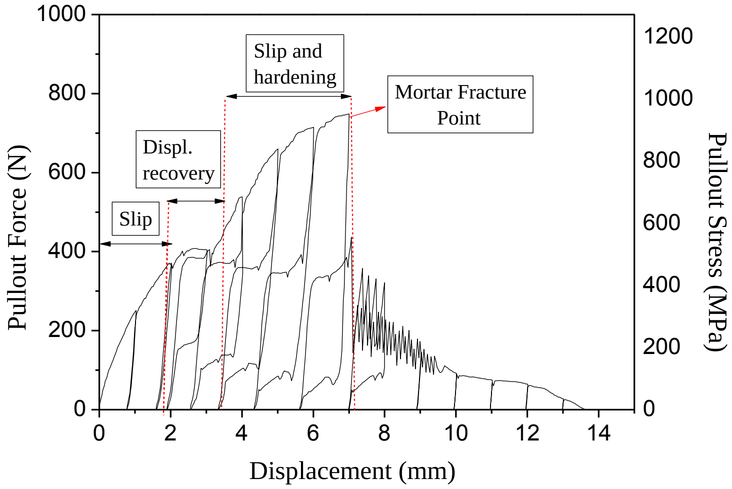

(c) Diameter of 1.0 mm

Fig. 9 Combined load-displacement-stress graphs for fiber with 5-mm spearhead

To provide a good insight into the pullout behavior of SE SMA fiber, the graphs given in Figs. 9(a) and 9(c) were designated as a representative on which different fiber pullout steps were indicated. As seen in Figs. 9(a) and 9(c), in the first part of the graphs for which the stress developed up to 400 MPa, the observed residual displacement may be attributed to the initial slip of the fiber. Afterward, the stress in fiber reached the upper plateau stress of 600 MPa, and the displacement could be recovered due to superelasticity, as indicated by displacement recovery on the graph. In the later part, stress-induced-martensite (SIM) hardening can be seen. The only difference between the two graphs is the failure part. For the graphs of fibers with diameters of 0.5 mm, failure occurred due to breakage of fiber while for the fiber of 1.0 mm diameter, failure occurred due to the cracking and destruction of the specimen. Therefore, the fiber could not carry any more load as indicated by a drop in the graph. It should be noted that the pullout behavior of the fiber with a 0.7 mm diameter is similar to that of the fiber with a 0.5 mm diameter.

The stress developed in the SMA fiber during the pullout test, which is called pullout stress, can be obtained by dividing the pullout force by the cross-sectional area of the fiber. The pullout test on the specimen having the fiber of 0.5 mm diameter resulted in the average maximum pullout load of 266 N and corresponding stress of 1357 MPa at the displacement of 3.33 mm.

The maximum pullout load of 459 N and the corresponding stress of 1193 MPa at the displacement of 5.34 mm were obtained for the specimen with the SE SMA fiber of 0.7 mm diameter. After a tensile load was applied to the fiber of 1.0 mm diameter embedded in the cementitious mortar, the maximum pullout load of 726 N and pullout stress of 924 MPa were obtained for which the displacement of 6.73 mm occurred.

4.2 Crimped length of 10 mm

The combined load-displacement-stress graphs expressing the pullout behavior of fibers with a spearhead

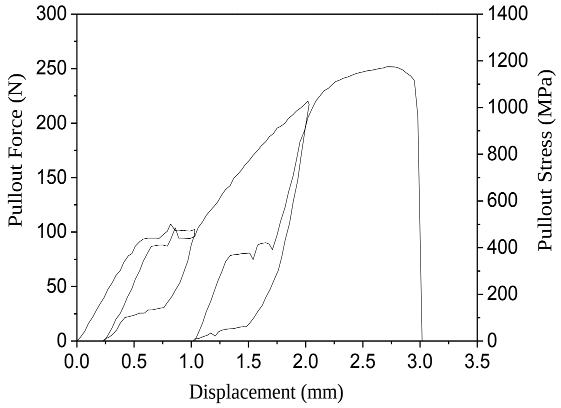

(a) Diameter of 0.5 mm

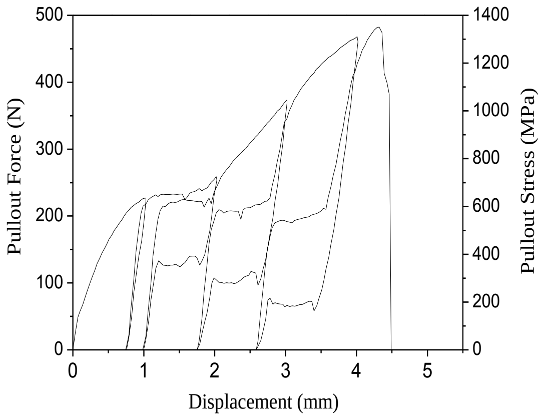

(b) Diameter of 0.7 mm

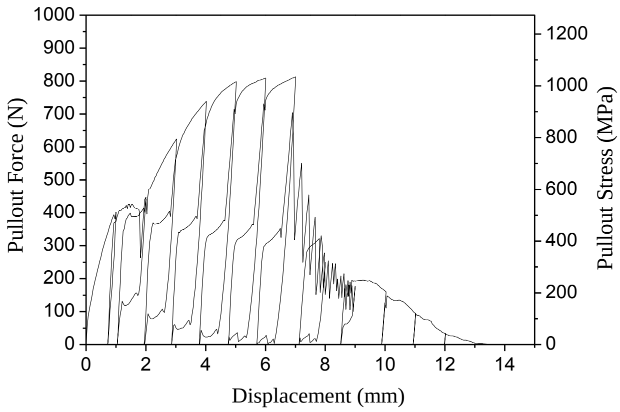

(c) Diameter of 1.0 mm

Fig. 10 Combined load-displacement-stress graphs for fiber with 10mm spearhead

end of 10 mm length are provided in Fig. 10. It should be noted that the same pullout behavior was observed as that of the fibers with 5.0 mm spearhead ends.

The average maximum pullout load of 252 N was achieved for the SE SMA fiber of 0.5 mm diameter while the maximum stress of 1283 MPa at the displacement of 2.78 mm was observed. The maximum pullout load of 482 N and the corresponding stress of 1252 MPa and displacement of 4.32 mm were obtained for the specimen with the SE SMA fiber of 0.7 mm diameter. Applying a tensile load to the fiber of 1.0 mm diameter yielded the maximum pullout load of 813 N and pullout stress of 1035 MPa while the corresponding displacement of 7.01 mm occurred. Superelasticity was activated and flag-shaped behavior occurred when the stress increased above the upper plateau stress of 620 MPa. After the maximum load, no sudden drop is seen in the graph in the Fig. 10(c). Fiber slip occurred and resulted in residual strain or permanent displacement. As seen in Fig. 10(c), during pullout test, the fiber almost fully slipped, and the load-bearing capacity gradually decreased with respect to fiber displacement.

4.3 Displacement recovery ratio (DRR)

The recovered displacement was normalized by dividing it by the loading displacement related to each step and was represented by displacement recovery ratio (DRR). Fig. 11 shows the DRRs of the spearhead fibers of the two main batches of wires with 5 and 10 mm crimped lengths. As seen in the graphs, no perfect displacement recovery (a 100% DRR) was observed for any of the types of the fibers. For the batch of fibers with 5 mm spearhead ends, the fiber with 0.5 mm diameter resulted in the highest DRR over 80% at a 2 mm displacement as shown in Fig. 11(a). Other types were less effective in displacement recovery. The highest DRR of 80% was obtained for the fiber of 0.7 mm diameter at 2 mm displacement from the batch of fibers with 10 mm spearhead ends. The fiber of 0.5 mm diameter provided a displacement recovery very close to that of the fiber of 0.5 mm diameter. It can be inferred that they recovered the displacement with almost the same DRR. As seen in Fig. 11, before a crack appeared in the cementitious mortar and caused the mortar to fracture, all the specimens could provide an acceptable displacement recovery, but after cracking, the DRR reduced to almost zero for all types except for the fiber with 0.7 mm diameter. However, they

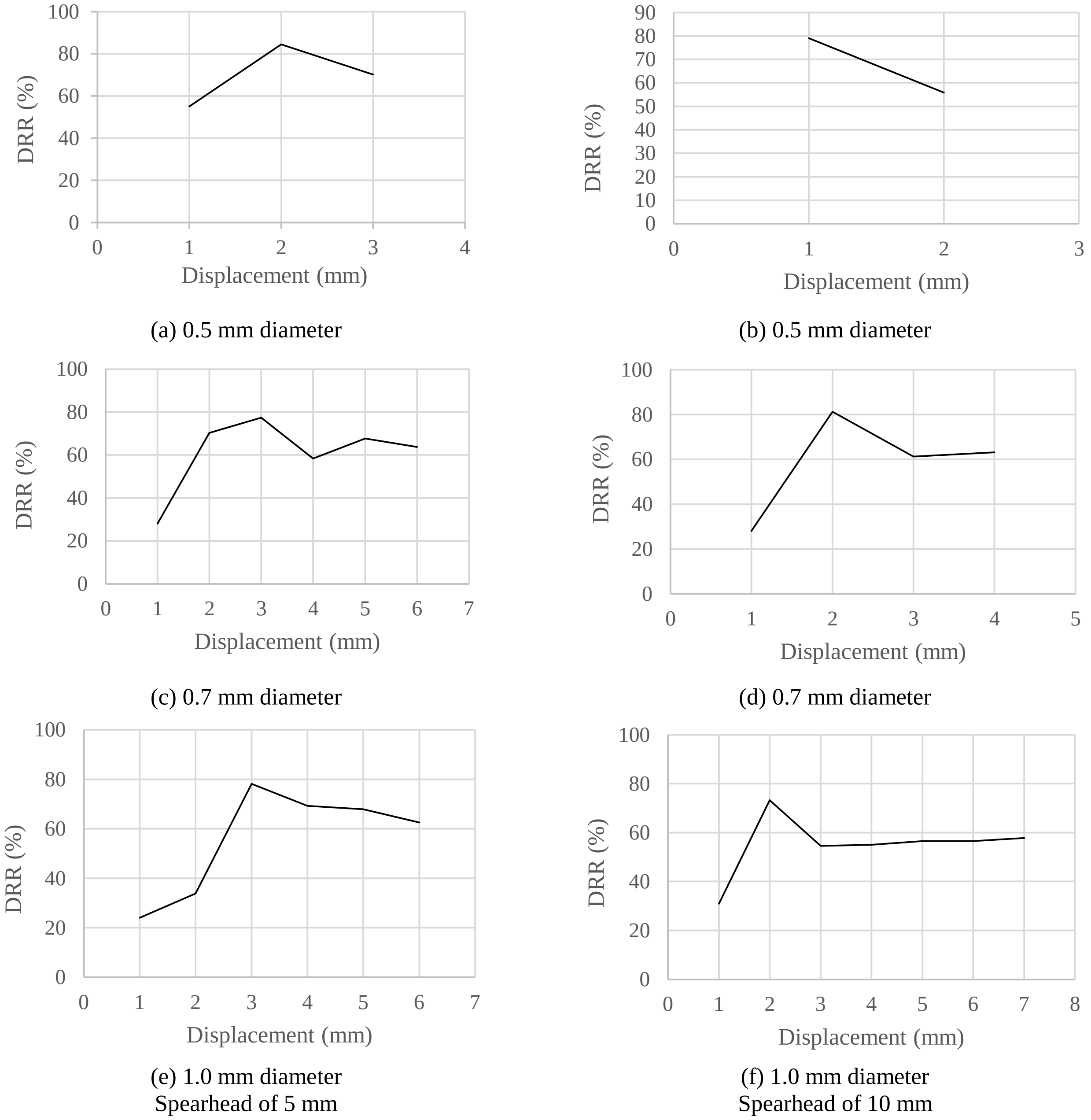

(a) 0.5 mm diameter

(b) 0.5 mm diameter

(c) 0.7 mm diameter

(d) 0.7 mm diameter

(e) 1.0 mm diameter
Spearhead of 5 mm

(f) 1.0 mm diameter
Spearhead of 10 mm

Fig. 11 Displacement recovery ratio for two main batches of SE SMA fibers

followed approximately the same trend such that an increase in DRR can be seen until the maximum amount, which occurred just before cracking. Later on, it was followed by a decrease in DRR. This demonstrates that the existence of a crack resulted in a decrease in self-centering capacity and load-bearing capacity.

As seen in Fig. 11, the graphs do not begin from the origin, and at the starting point, an initial displacement can be seen. This is because of initial slip, which occurs due to the geometry of the fiber end. After a small slip, the fiber griped in the cementitious mortar and the stress induced in the fiber developed to upper plateau stress, so, superelasticity was activated and displacement could be recovered.

5. Discussions

5.1 Pullout behavior

The results of the pullout test on the specimen including the fiber of 0.5 mm diameter with a 5 mm crimped-end length showed that as fiber slip occurred, the bond strength between the fiber and cementitious mortar was degraded; thus, it could not carry additional pullout load and the frictional resistance was reduced with a decrease in the embedded length. Upon application of the maximum pullout load, the chemical adhesion disappeared, and the bond strength was destroyed. After the stress in the SMA fiber developed beyond the upper plateau stress of 655 MPa, flag-shape behavior was observed. Therefore, the self-centering capacity was activated, and the fiber displacement was recovered.

For the fiber of 0.7 mm diameter with a 5 mm crimped end length, the stress in the fiber developed beyond the upper plateau stress of 653 MPa. Therefore, superelasticity was activated and flag-shaped behavior was observed. For this type, the fiber slip also resulted in a decrease in bond strength. After the maximum load was applied, it was suddenly destroyed, after which no more pullout load could be carried. As seen in the graph, despite flag-shaped behavior, permanent displacement (plastic displacement) occurred. A reason for this is that the displacement is the sum of fiber slip and deformation. After each load cycle, deformation was recovered because of superelasticity, but fiber slip remained; therefore, plastic displacement was observed.

For the specimen including the fiber with 1.0 mm diameter and 5 mm spearhead length, superelasticity was activated and flag-shaped behavior was observed as the stress increased above the upper plateau stress of 620 MPa. After the maximum load was applied, as the displacement increased, the bond strength between fiber and the cementitious mortar and the load-bearing capacity gradually decreased, and no sudden drop was seen. For this type, plastic displacement was also observed due to fiber slip. The pullout test continued until all the embedded length of the fiber almost slipped.

The results of the pullout test on specimens with a spearhead length of 10 mm are shown in Fig. 10. Like the fibers with 5 mm spearhead length, it was observed that the bond between the fibers and cementitious mortar was gradually weakened, but a sudden drop occurred after the maximum load was applied. Despite having activated self-centering and flag-shaped behavior, a perfect displacement recovery was not achieved. However, compared with the fibers with the crimped end of 5 mm length, they could not provide a better flag-shaped behavior, and plastic deformation was still observed.

In general, the pullout behavior of the SE SMA fibers can be divided into three parts; namely, 1) initial slipping range, 2) recovering range, and 3) hardening and slipping range. The first initial slipping range continued until the stress of the SMA fiber reached the upper plateau stress. In the range, all residual displacement was due to the slip of the fiber because the SMA fiber was in the elastic range; thus, its elastic deformation was totally recovered. Therefore, in this range, as shown in Fig. 11, the DRRs of the fibers were relatively low because of the fiber slip (permanent displacement). The second recovering range occurred when the fiber reached the upper plateau stress. In this range, the SMA fiber showed superelastic behavior; thus, the pullout behavior became flag-shaped. Because of this superelastic behavior, the fiber showed good self-centering capacity (recovering displacement), and the DRR increased to 80%. The third hardening and slipping range occurred when the stress of the fiber exceeded the upper plateau stress. Thus, the fiber entered into the stress-induced-martensitic hardening range. As a result, residual deformation remained in the fiber, and the anchoring action did not bear the developed force in the fiber; this triggered slipping. Therefore, the pullout behavior was still flag-shaped, but the residual displacement increased with more loading displacement. Thus, in this range, the displacement consisted of pure slip and residual deformation of the fiber. After the maximum pullout force developed, the fiber was fractured, or the mortar was broken; therefore, the pullout force dropped abruptly. Based on these observations, the stress of the SE SMA fiber should be controlled not to exceed the upper plateau stress so that the fiber will show good self-centering capacity.

5.2 Comparison

Pullout tests were conducted to assess SMA fiber pullout resistance with respect to fiber end shape length and fiber diameter. Two types of comparisons were made to gain insight into the effects of SE SMA fiber geometrical parameters on the bond strength between the fiber and mortar, pullout load bearing capacity, and displacement recovery of the fiber through its self-centering property. The pullout stress results for the various fiber diameters for each spearhead length were compared. For this aim, a quantitative parameter, maximum bond stress τ_{max}, was considered as given in Eq. (1)

$$\tau_{max} = {P_{max}}/{\pi d_f L_{em}} \tag{1}$$

where P_{max} is the maximum pullout force, d_f is the fiber diameter, and L_{em} is the fiber embedded length. From Eq. (1), it was found that the maximum bond strength is a function of the maximum pullout force. Fig. 12 compares the maximum pullout stress values obtained for the various types of fibers.

Fig. 12(a) compares the pullout stress results demonstrating the effects of crimped length on pullout strength. From the figure, it can be inferred that for the smallest fiber size the highest pullout stress was achieved. As shown for the fiber of 5 mm length, the smaller crimped length resulted in a higher pullout stress induced in the fiber. For other cases, as expected, an increase in the length of the anchorage end resulted in enhanced pullout resistance. Formation of a crack at the interface of the fiber and cementitious mortar could result in a decrease in bond and fiber slip. As the embedded length of fibers is similar, the frictional force did not have a substantial effect. Actually, it can be concluded that an increase in the crimped end length could not enhance the bond strength and load carrying capacity.

The effects of fiber geometric parameters on the self-centering capacity of the fibers are shown in Fig. 12(b). For the 5 mm crimped length the fiber of 0.5 mm diameter provided the best displacement recovery, while in the batch of fibers with 10 mm crimped length, the fiber with 0.7 mm diameter provided the best performance. However, as differences among the displacement recovery of fibers, which was shown in the form of displacement recovery ratio (DRR), was small, it seems that the fiber diameter and crimped length did not have much influence on the self-centering capacity of the SE SMA fibers. Therefore, based

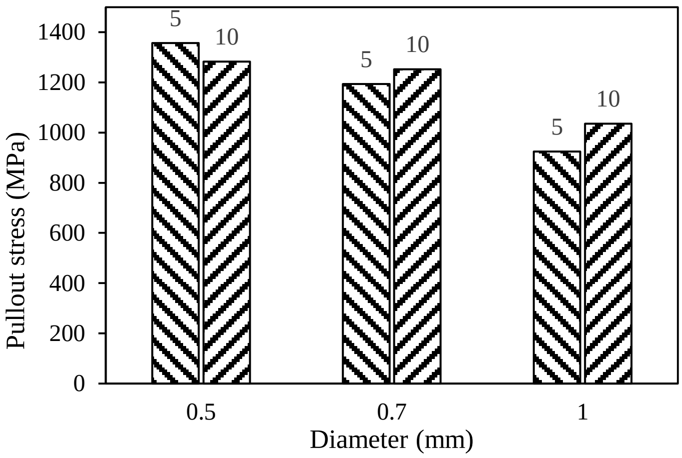

(a) Maximum pullout stress for both fiber diameter and crimped length

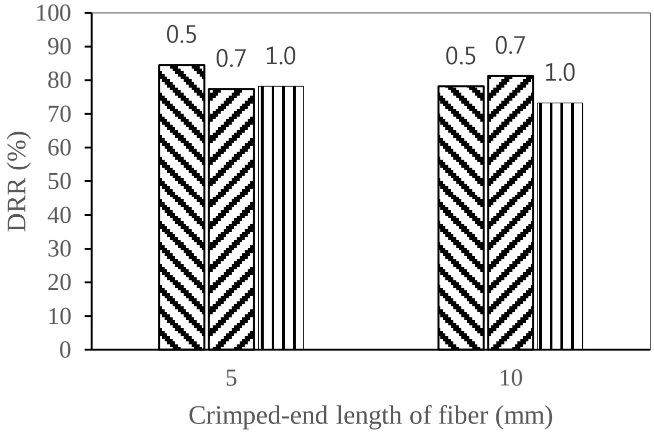

(b) Comparison of the self-centering capacity of SE SMA fibers

Fig. 12 Comparison of maximum pullout stress for evaluation of fiber geometric parameter effects on pullout resistance and displacement recovery

on the desired application, any size of fiber can be employed.

To have a better understanding of the pullout behavior of the SE SMA fiber, we attempted to calculate the pure slip and pure displacement of each type of fiber. The displacement of fiber was calculated based on the results obtained from the tensile test of SE SMA wire from which the fibers were manufactured. At each stress level, the corresponding strain could be obtained. Multiplying the strain by the total length of the fiber resulted in the corresponding pure deformation of the fiber. Subtracting the pure deformation from a total displacement of the fiber, the pure fiber slip was obtained. Knowing this could facilitate finding the weak points of the pullout resistance, such as whether the fiber slip should be further considered to be prevented or more consideration should be devoted to fiber deformation. For fiber slip, the fiber end shape can be chosen and created such that the minimum slip occurs, while for fiber deformation, a material can be used that yields smaller plastic deformation, i.e., a better superelasticity can be achieved.

Fig. 13 compares the total fiber displacement (fiber slip and deformation) and pure fiber slip. In Fig. 13, the abscissa indicates the number of loading–unloading cycles for which an amount of slip occurred, while the ordinate indicates the amount of slip that occurred for each loading–unloading cycle.

As seen in Fig. 13, at the initial loading cycles, the total displacement comes from the fiber slip, i.e., only fiber slip occurs. With the application of more loading cycles, the fiber deforms and it increases in length. Therefore, the total displacement consists of fiber slip and fiber deformation. The only exception is for the fiber of 1.0 mm diameter, for which at the later loading cycles and before the failure of the specimen, the fiber slips and sustains no more deformation. Therefore, the total displacement comes from fiber slip only

6. Conclusions

This study investigated the pullout resistance and self-centering capacity of superelastic SMA fibers considering effects of the crimped end (spearhead-shaped end) length and fiber diameter. For this purpose, a pullout test was

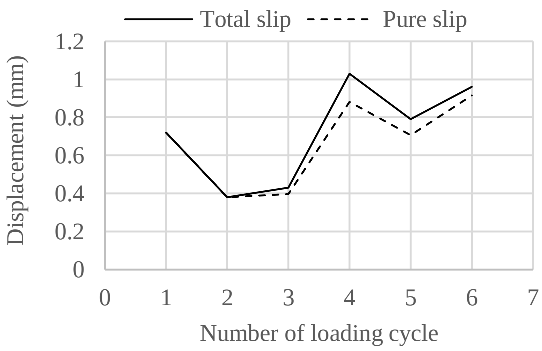

(a) 0.7 mm diameter

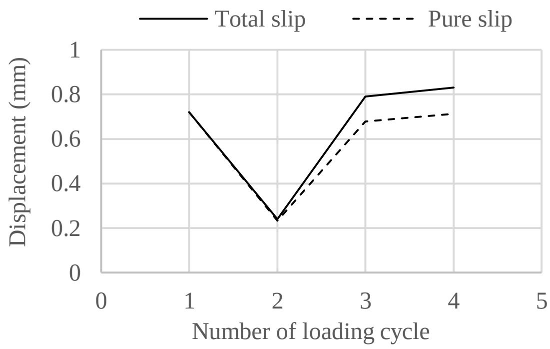

(b) 0.7 mm diameter

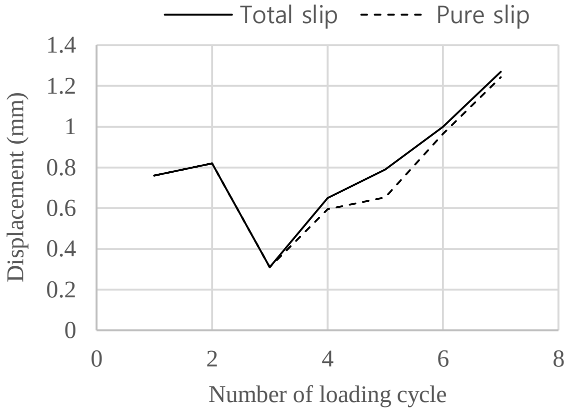

(c) 1.0 mm diameter
The spearhead of 5 mm

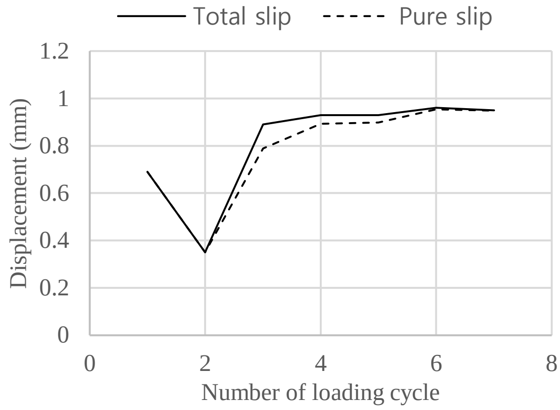

(d) 1.0 mm diameter
The spearhead of 10 mm

Fig. 13 Comparative graphs presenting total displacement, and pure slip

performed on single-fiber specimens. Specimens were fabricated in two main batches using fibers with crimped end lengths of 5 and 10 mm. Each batch was also divided into three subsets according to three diameters, namely, 0.5, 0.7, and 1.0 mm. The results of the pullout test on the fibers with 5 mm spearhead showed that the fiber of 0.5 mm diameter could provide the highest pullout stress, while the lowest stress belonged to the fiber of 1.0 mm diameter. The same trend was also observed for the batch of fibers with 10 mm crimped length. However, because the differences among the obtained results were small, it can be concluded that fiber diameter does not have much effect on the pullout resistance. A comparison of the obtained pullout stress results indicated that increase in the length of the crimped end had a negligible effect on the pullout resistance. Therefore, it can be suggested that spearhead fiber can be employed to provide anchoring action and enhance the pullout resistance of the fiber embedded in cementitious mortar regardless of the crimped length. Investigating the displacement recovery of the SE SMA fibers showed that the geometric parameters of the fibers did not have a significant effect on their self-centering capacity. It can be concluded that, based on the application and SMA fiber availability, any dimension of spearhead fiber can be employed. For practical applications, small fibers can be used with respect to the size of the structural member. Using small fibers helps to provide a bigger interface of fiber and matrix and higher frictional force and bond strength. Moreover, because small fibers can be more distributed through the cement mortar, they can close more cracks than larger fibers. In the case of large structural members, larger fibers can be used to reduce the number of fibers to be fabricated.

The results showed that as the pullout test started, the fiber slipped at the initial step due to the geometry of the fiber end. Then, the fiber was stuck in the cementitious mortar, and through the development of stress in the fiber, superelasticity was activated and displacement was recovered. Thereafter, SIM hardening occurred, and after displacement recovery, a residual strain was observed, showing that the fiber underwent plastic deformation. Finally, a drop was seen in the load-displacement and DRR graphs because of specimen failure. The total pullout behavior of the fiber can be summarized as follows. The fiber experienced slip at the initial loading–unloading cycles, then it sustained deformation, and finally, the fiber tolerated slip and the specimen failed. It should be noted that to have a good self-centering capacity, the stress in the SE SMA fiber should not develop beyond the upper plateau stress.

Acknowledgments

This research was supported by the Basic Science Research Program through the National Research

Foundation of Korea (NRF) funded by the Ministry of Education, Science and Technology (Project No. 2015-041523).

References

Abou-Elfath, H. (2017), "Evaluating the ductility characteristics of self-centering buckling-restrained shape memory alloy braces", *Smart Mater. Struct.*, **26**(5), 055020.

Aguirre, D.A. and Montejo, L.A. (2014), "Damping and frequency changes induced by increasing levels of inelastic seismic demand", *Smart Struct. Syst.*, **14**(3), 445-468. http://dx.doi.org/10.12989/sss.2014.14.3.445.

Baghani, M., Naghdabadi, R., Arghavani, J. and Sohrabpour, S. (2012), "A thermodynamically-consistent 3D constitutive model for shape memory polymers", *Int. J. Plasticity*, **35**, 13-30. https://doi.org/10.1016/j.ijplas.2012.01.007.

Choi, E., Chae, S.W., Park, H., Nam, T.H., Mohammadzadeh, B. and Hwang, J.H. (2018), "Investigating self-centering capacity of superelastic shape memory alloy fibers with different anchorages through pullout tests", *J. Nanosci. Nanotechno.*, **18**, 6228-6232. https://doi.org/10.1166/jnn.2018.15635.

Choi, E., Cho, B.S. and Lee, S. (2015), "Seismic retrofit of circular RC columns through using tensioned GFRP wires winding", *Compos. Part B: Eng.*, **83**, 216-225. https://doi.org/10.1016/j.compositesb.2015.08.041.

Choi, E., Kim, D.J., Chung, Y.S., Kim, H.S., and Jung, C. (2015), "Crack-closing of cement mortar beams using NiTi cold-drawn SMA short fibers", *Smart Mater. Struct.*, **24**(1), 015018.

Choi, E., Kim, D.J., Hwang, J.H. and Kim, W.J. (2016), "Prestressing effect of cold-drawn short NiTi SMA fibers in steel reinforced mortar beams", *Smart Mater. Struct.*, **25**(8), 085041.

Choi, E., Kim, D.J., Jeon, C. and Gin, S. (2016), "New SMA short fibers for cement composites manufactured by cold drawing", *J. Mater. Sci. Res.*, **5**(2), 74-87.

Choi, E., Kim, D.J., Lee, J.H. and Ryu, G.S. (2017), "Monotonic and hysteretic pullout behavior of superelastic SMA fibers with different anchorages", *Compos. Part B: Eng.*, **108**, 232-242. https://doi.org/10.1016/j.compositesb.2016.09.080.

Choi, E., Kim, D.J., Youn, H. and Nam, T.H. (2015), "Repairing cracks developed in mortar beams reinforce by cold-drawn NiTi or NiTiNb SMA fibers", *Smart Mater. Struct.*, **24**(12), 125010.

Choi, E., Mohammadzadeh, B., Hwang, J.H. and Kim, W.J. (2018), "Pullout behavior of superelastic SMA fibers with various end-shapes embedded in cement mortar", *Constr. Build. Mater.*, **167**, 605-616. https://doi.org/10.1016/j.conbuildmat.2018.02.070.

Choi, E., Mohammadzadeh, B., Kim, D. and Jeon, J.S. (2018), "A new experimental investigation into the effects of reinforcing mortar beams with superelastic SMA fibers on controlling and closing cracks", *Compos. Part B: Eng.*, **137**, 140-152. https://doi.org/10.1016/j.compositesb.2017.11.017.

Dyshlyuk, A.V., Makarova, N.V., Vitrik, O.B., Kulchin, Y.N. and Babin, S.A. (2017), "Strain monitoring of reinforced concrete with OTDR-based FBG interrogation technique", *Smart Struct. Syst.*, **20**(3), 343-350. https://doi.org/10.12989/sss.2017.20.3.343.

Farmani, M.A. and Ghassemieh, M. (2016), "Shape memory alloy-based moment connections with superior self-centering properties", *Smart Mater. Struct.*, **25**(7), 075028.

Feng, X.Q. and Sun, Q. (2007), "Shakedown analysis of shape memory alloy structures", *Int. J. Plasticity*, **23**(2), 183-206. https://doi.org/10.1016/j.ijplas.2006.04.001.

Gribniak, V., Rimkus, A., Torres, L. and Hui, D. (2018), "An experimental study on cracking and deformations of tensile concrete elements reinforced with multiple GFRP bars", *Compos. Struct.*, **201**, 477-485. https://doi.org/10.1016/j.compstruct.2018.06.059.

Hadi, A. and Akbari, H. (2016), "Modeling and control of a flexible continuum module actuated by embedded shape memory alloys", *Smart Struct. Syst.*, **18**(4), 663-682. http://dx.doi.org/10.12989/sss.2016.18.4.663.

Horney, L., Chlup, V.H., Janouchova, K. and Vysanska, M. (2012), "Single fiber pull-out test of nitinol-silicon-textile composite", *Bull. Appl. Mech.*, **8**(32), 77-80.

Jang, K. and An, Y.K. (2018), "Multiple crack evaluation on concrete using a line laser thermography scanning", *Smart Struct. Syst.*, **22**(2), 201-207. https://doi.org/10.12989/sss.2018.22.2.201.

Jiang, Z., Li, W. and Yuan, Z. (2015), "Influence of mineral additives and environmental conditions on the self-healing capabilities of cementitious materials", *Cement Concrete Compos.*, **57**, 116-127. https://doi.org/10.1016/j.cemconcomp.2014.11.014.

Kabir, M.R., Alam, M.S., Said, A.M. and Ayad, A. (2016), "Performance of hybrid reinforced concrete beam column joint: A critical review", *Fibers*, **4**(13), 1-12, doi:10.3390/fib4020013.

Kang, M.S., An, Y.K. and Kim, D.J. (2018), "Electrical impedance-based crack detection of SFRC under varying environmental conditions", *Smart Struct. Syst.*, **22**(1), 1-11. https://doi.org/10.12989/sss.2018.22.1.001.

Kim, B. and Cho, S. (2018), "Efflorescence assessment using hyperspectral imaging for concrete structure", *Smart Struct. Syst.*, **22**(2), 209-221. https://doi.org/10.12989/sss.2018.22.2.209.

Kim, D.J., Kim, H.A., Chung, Y.S. and Choi, E. (2014), "Pullout resistance of straight NiTi shape memory alloy fibers in cement mortar after cold drawing and heat treatment", *Compos. Part B*, **67**, 588-594. https://doi.org/10.1016/j.compositesb.2014.08.018.

Kim, H.Y., Ikehara, Y., Kim, J.I., Hosoda, H. and Miyazaki, S. (2006), "Martnesitic transformation, shape memory effect and superelasticity of Ti-Nb binary alloys", *Acta Materialia*, **54**(9), 2419-2429. https://doi.org/10.1016/j.actamat.2006.01.019.

Kim, W.J., Lee, J.M., Kim, J.S. and Lee, C.J. (2012), "Measuring high speed crack propagation in concrete fracture test using mechanoluminescent material", *Smart Struct. Syst.*, **10**(6), 547-555. http://dx.doi.org/10.12989/sss.2012.10.6.547.

Li, X., Li, M., and Song, G. (2015), "Energy-dissipating and self-repairing SMA-ECC composite material system", *Smart Mater. Struct.*, **24**(2), 025024.

Liu, J.L., Huang, H.Y. and Xie, J.X. (2015), "Superelastic anisotropy characteristics of columnar-grained Cu-Al_Mn shape memory alloys and its potential applications", *Mater. Design*, **85**, 211-220. https://doi.org/10.1016/j.matdes.2015.06.114.

Mehrabi, R. and Karamooz Ravari, M.R. (2015), "Simulation of superelastic SMA helical springs", *Smart Struct. Syst.*, **16**(1), 183-194. http://dx.doi.org/10.12989/sss.2015.16.1.183.

Mohammadzadeh, B. and Noh, H.C. (2014), "Use of buckling coefficients in predicting buckling load of plates with and without holes", *J. Korean Soc. Adv. Copm. Struct.*, **5**(3), 1-7. http://dx.doi.org/10.11004/kosacs.2014.5.3.001.

Mohammadzadeh, B. and Noh, H.C. (2015), "Numerical analysis of dynamic responses of the plate subjected to impulsive loads", *Int. J. Civil, Environ. Struct. Constr. Architect. Eng.*, **9**(9), 1148-1151.

Mohammadzadeh, B. and Noh, H.C. (2016), "Investigation into buckling coefficients of plates with holes considering variation of hole size and plate thickness", *Mechanika*, **22**(3), 167-175. https://doi.org/10.5755/j01.mech.22.3.12767.

Mohammadzadeh, B. and Noh, H.C. (2017), "Analytical method to investigate nonlinear dynamic responses of sandwich plates

with FGM faces resting on elastic foundation considering blast loads", *Compos. Struct.*, **174**, 142-157. https://doi.org/10.1016/j.compstruct.2017.03.087.
Mohammadzadeh, B. and Noh, H.C. (2019), "An analytical and numerical investigation on the dynamic responses of steel plates considering the blast loads", *Int. J. Steel Struct.*, **19**(2),603-617.
Mohammadzadeh, B., Bina, M. and Hasounizadeh, H. (2012), "Application and comparison of mathematical and physical models on inspecting slab of stilling basin floor under static and dynamic forces", *Appl. Mech. Mater.*, **147**, 283-287. https://doi.org/10.4028/www.scientific.net/AMM.147.283.
Oudah, F. and El-Hacha, R. (2017), "Joint performance in concrete beam-column connections reinforced using SMAsmart material", *Eng. Struct.*, **151**, 745-760. https://doi.org/10.1016/j.engstruct.2017.08.054.
Pereiro-Barcelo, J. and Bonet, J. (2017), "Ni-Ti SMA bars behaviour under compression", *Constr. Build. Mater.*, **155**, 348-362. https://doi.org/10.1016/j.conbuildmat.2017.08.083.
Qiu, C., Zhang, Y., Qi, J. and Li, H. (2018), "Seismic behavior of properly designed CBFs equipped with NiTi SMA braces", *Smart Struct. Syst.*, **21**(4), 479-491. https://doi.org/10.12989/sss.2018.21.4.479.
Schrooten, J., Michaud, V., Parthenios, J., Psarras, G.C., Galiotis, C., Gotthardt, R., Manson, J.A. and Humbeeck, J.V. (2002), "Progress on composites with embedded shape memory alloy wires", *Materials Transactions, Special Issue on Smart Materials Fundamentals and Applications*, **43**(5), 961-973.
Shahverdi, M., Czaderski, C. and Motavalli, M. (2016), "Iron-based shape memory alloys for prestressed near- surface mounted strengthening of reinforced concrete beams", *Constr. Build. Mater.*, **112**, 28-38. https://doi.org/10.1016/j.conbuildmat.2016.02.174.
Shokri, T. and Nanni, A. (2014), "Crack source location by acoustic emission monitoring method in RC strips during in-situ load test", *Smart Struct. Syst.*, **13**(1), 155-171. http://dx.doi.org/10.12989/sss.2014.13.1.155.
Truong, B.T., Bui, T.T., Limam, A., Larabi, A.S., Nguyen, K.L. and Michel, M. (2017), Experimental investigations of reinforced concrete beams repaired/reinforcd by TRC composites", *Compos. Struct.*, **168**, 826-839. https://doi.org/10.1016/j.compstruct.2017.02.080.
Wang, J., Sehitoglu, H. and Maier, H.J. (2014), "Dislocation slip stress prediction in shape memory alloys", *Int. J. Plasticity*, **54**, 247-266. https://doi.org/10.1016/j.ijplas.2013.08.017.
Yang, M., Feng, L., Gu, H., Su, H., Cui, X. and Cao, W. (2017), "Crack detection study for hydraulic concrete using PPP-BOTDA", *Smart Struct. Syst.*, **20**(1), 75-83. https://doi.org/10.12989/sss.2017.20.1.075.

HJ